AGU100 ADVANCING EARTH AND SPACE SCIENCE

Water Resources Research

RESEARCH ARTICLE
10.1029/2018WR024470

Key Points:
- Laboratory studies of solute transport in heterogeneous porous media under dynamic boundary conditions are conducted
- Combination of dynamic boundary conditions and material heterogeneity affects solute leaching in experiments and can induce strong tailing
- Study highlights importance of consideration of dynamic boundary conditions in predictions of solute leaching

Correspondence to:
C. J. M. Cremer,
cremer@hydromech.uni-hannover.de

Citation:
Cremer, C. J. M., & Neuweiler, I. (2019). How dynamic boundary conditions induce solute trapping and quasi-stagnant zones in laboratory experiments comprising unsaturated heterogeneous porous media. *Water Resources Research*, *55*, 10,765–10,780. https://doi.org/10.1029/2018WR024470

Received 25 NOV 2018
Accepted 15 OCT 2019
Accepted article online 23 NOV 2019
Published online 13 DEC 2019

How Dynamic Boundary Conditions Induce Solute Trapping and Quasi-stagnant Zones in Laboratory Experiments Comprising Unsaturated Heterogeneous Porous Media

C. J. M. Cremer[1] **and I. Neuweiler**[1]

[1]Leibniz Universität Hannover, Institute of Fluid Mechanics and Environmental Physics in Civil Engineering, Hanover, Germany

Abstract The vadose zone is subject to dynamic boundary conditions in the form of infiltration and evaporation. A better understanding of implications for flow and solute transport, arising from these dynamic boundary conditions in combination with heterogeneous structure, will help to improve the prediction of the fate of solutes. We present laboratory experiments and numerical simulations of heterogeneous porous media under unsaturated conditions where controlled, temporally varying precipitation and evaporation are applied to study the effect of dynamic boundary conditions on solute transport in the presence of material interfaces. Dye tracers Eosine Y and Brilliant Blue FCF are utilized to visualize solute transport and analyze redistribution processes in a flow cell. Water and solute fluxes in and out of the flow cell are quantified. While in dynamic experiments application of small infiltration rates (significantly below the saturated hydraulic conductivities of the materials) led to a reversal of transport paths between infiltration and succeeding evaporation, larger infiltration rates altered downward transport such that flow and transport paths differed from those observed during evaporation. Differences in transport paths ultimately led to a redistribution and trapping of solute in one material which manifested as pronounced tailing in breakthrough curves. Trapping was induced not by the formation of a stagnant zone as result of large parameter contrast but by an interplay of dynamic boundary conditions and material heterogeneity. This study thereby highlights the importance to consider dynamic boundary conditions in predictions of solute leaching.

1. Introduction

Knowledge of water and solute movement in shallow subsurface of the earth is crucial for the assessment of risks related to contaminant spills, for planning remediation strategies and hence for preservation of groundwater and soil resources (van Dam et al., 2004).

The shallow subsurface is characterized by spatial heterogeneity of soil properties which affect water flow and solute transport (Kasteel et al., 2009; Roth, 1995; Roth & Hammel, 1996). Additionally, transient boundary conditions induce temporally varying water distribution and thus affect soil hydraulic properties such as the unsaturated hydraulic conductivity. The superposition of transient boundary conditions, heterogeneous soil structure, and spatiotemporally changing hydraulic properties thereby determines flow and transport paths and directions in the vadose zone.

Studies of the complicated interplay of structural heterogeneity and transient boundary conditions on solute transport in the vadose zone are in most studies limited either to the process of infiltration (downward flow) (Wildenschild & Jensen, 1999) or evaporation (upward flow) (Bechtold et al., 2012; Lehmann & Or, 2009; Nachshon et al., 2011). While solute transport for these specific conditions is well studied and relatively well understood, less attention has been paid on the coherent investigation of infiltration and evaporation in cycles and possible implications for solute transport.

Numerical investigations of three-dimensional unsaturated flow and transport at the field scale with changing flux direction have been conducted by Russo et al. (1998). Heterogeneity in this study was induced by a stochastic (Gaussian) distribution of soil properties. Realistic weather conditions as well as rootwater uptake were considered. For simulations comprising dynamic boundary conditions, compared

to steady-state infiltration, Russo et al. (1998) observed an earlier solute breakthrough, higher peak concentrations, and longer tailing along with reduced skewness of the breakthrough curve.

These findings were later confirmed in a numerical study by Vanderborght et al. (2006). In addition, larger transversal redistribution of solute was observed for simulations comprising dynamic boundary conditions. Russo and Fiori (2008) investigated the applicability of an equivalent steady-state flow model to results obtained from a transient numerical model very similar to the one utilized in Russo et al. (1998). They found that the applicability depended on the distance between soil surface and groundwater table, where for sufficiently large distances, the steady-state model may be applicable. This result was found to be valid for different textures, vegetation, and atmospheric conditions. Regarding the solute breakthrough, results were found to be in agreement with those obtained by Russo et al. (1998). In a recent publication, Cremer et al. (2016) conducted a two-dimensional numerical study to assess the effect of intensity and duration of cyclic infiltration and evaporation on solute transport behavior in bimodal porous media. To isolate the effect of the dynamics of the atmospheric boundary condition, cycles of infiltration and evaporation with differing rates and durations but comparable cycle averaged net flux were compared. Heterogeneity was induced by vertical layers of (i) two porous materials as in Lehmann and Or (2009) and Bechtold, Haber-Pohlmeier, et al. (2011) and (ii) by structured fields. It was illustrated that dynamic boundary conditions can, depending on precipitation duration and intensity, significantly affect solute leaching. In accordance with numerical and laboratory studies performed by Bechtold, Haber-Pohlmeier, et al. (2011), lateral solute redistribution through material interfaces, controlled mainly by the local unsaturated hydraulic conductivity curves of the individual materials, was found to play a key role for solute leaching. Another important factor was found to be the orientation and arrangement of materials. In accordance to findings by Schlueter et al. (2012), vertical continuous layers oriented parallel to the mean flow direction enhanced the impact of dynamic boundary conditions, while the structured field led to more variability in the flow field and enhanced macrodispersion.

The aforementioned numerical studies find that dynamic boundary conditions may alter flow and transport paths within heterogeneous porous media. This change of paths eventually results in faster or retarded solute leaching. However, these findings are based on assumptions in the conceptualization of the underlying models, in particular on the assumption of a spatially uniform evaporation and infiltration flux from a heterogeneous material surface. Furthermore, the role of transport in lateral crossflows is important. Transport on the twisted flow paths is modeled with the standard transport equation. In the vadose zone, the validity of transport mechanisms in the standard model, such as macrodispersion, is debated. Laboratory experiments that would be important to verify assumptions made in numerical simulations and confirm findings are scarce. A rare exception are the physical laboratory experiments conducted by Bechtold, Haber-Pohlmeier, et al. (2011) on solute transport in a cylindrical column filled with two partly saturated sands arranged with a sharp vertical interface. Dye and salt tracer distribution were monitored via magnetic resonance imaging, and evaporation fluxes were derived from infrared surface temperature measurements. Experiments comprising an infiltration followed by an evaporation were carried out. Bechtold, Haber-Pohlmeier, et al. (2011) found lateral solute redistribution between materials during upward transport, which potentially influences leaching behavior during subsequent infiltration events. Additionally, almost uniform evaporation fluxes from heterogeneous media were found.

Laboratory experiments considering dynamic boundary conditions comprising multiple infiltration evaporation cycles in which redistribution processes are assessed and solute leaching from heterogeneous materials is quantified are, however, missing.

In this manuscript we present well-controlled laboratory experiments in quasi two-dimensional, variably saturated porous media with well-defined heterogeneity where we applied dynamic boundary conditions in the form of infiltration-evaporation cycles. We used dye tracers to obtain measurements of solute breakthrough at the bottom of our domain along with photographic images of tracer distributions in the domain at different time steps. While the former observations present quantitative information, with the latter, we aim to capture the dynamics of the flow paths as well as solute transport and redistribution processes within the domain in a qualitative manner. Qualitative and quantitative indicators are evaluated jointly to understand how dynamic boundary conditions in interplay with material heterogeneity influence solute travel times and distributions.

Studies of solute mixing in saturated (groundwater) systems found that temporal fluctuations transversal to the main flow direction (i.e., in meandering paths) alter dispersion by enhancing its transversal and reducing

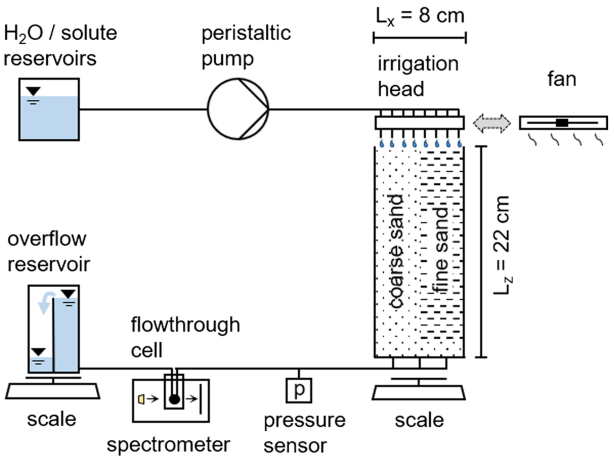

Figure 1. Sketch of laboratory setup including flow cell (with inner dimensions), arrangement of materials, and control and measurement devices.

its lateral component, while fluctucations parallel to the main flow direction have only negligible impact (Cirpka & Attinger, 2003; Dentz & Carrera, 2003; Rehfeldt & Gelhar, 1992). Based on those findings, our working hypothesis is that dynamic boundary conditions will most significantly affect solute transport when flow paths yield strong transversal components and differ between downward (infiltration) and upward (evaporation) periods. Consequently with this publication, we aim to provide a detailed documentation and assessment of laboratory experiments under well-defined laboratory conditions which is currently absent or at least rare in the literature, albeit necessary to fully understand and validate transport processes in the vadose zone. We specifically aim to illustrate and evaluate the effect of flow and transport paths which differ between infiltration and evaporation and the resulting effects on solute breakthrough.

Key factors to initiate a change in flow paths in variably saturated porous media are the materials local unsaturated hydraulic conductivities (depending on water content) and applied flow rates. The latter were deliberately varied in our study in order to compare settings with changing upward and downward flow paths to settings where flow paths do not change.

2. Experimental Setup

2.1. Flow Cell and Porous Media Properties and Initial and Boundary Conditions

2.1.1. Flow Cell

We carried out experiments of solute transport through unsaturated, heterogeneous porous media in transparent plexiglas flow cells with inner dimensions of 1 by 8 by 22 cm^3 (length by width by height) filled to a height of ≈21.5 cm with two types of quartz sand (FH31 and F36 from Quartzwerke Frechen), illustrated in Figure 1. Undisturbed outflow of water and solute at the bottom of the flow cell was ensured by three uniformly distributed outlets ($d = 5$ mm), covered with a highly permeable polyamid membrane to prevent outflow of grains without hindering flow. The topside of the flow cell was open, while all side walls were impermeable for water flow and solute transport.

2.1.2. Porous Media and Heterogeneous Structure

Similar to recent numerical studies (Bechtold, Haber-Pohlmeier, et al., 2011; Cremer et al., 2016; Lehmann & Or, 2009), heterogeneity was induced by a sharp vertical interface between both sands where each of the sands had a lateral extent of 4 cm (Figure 1). This structure presents a simplification of natural three-dimensionally connected structures but is beneficial due to its simplicity, allowing the identification of fundamental transport mechanisms. To ensure liquid phase continuity at the lower boundary, a ≈ 2 cm thick layer of the finer sand (F36) with high capillary suction was introduced at the bottom of the domain. The sands were packed under dry conditions with templates and carefully compacted by light vibrations. CT scans showed that this way of packing produces a sharp, barely mixed interface (not shown). Premeasured material properties for the individual utilized sands can be found in Table 1.

We deliberately utilized materials with a small contrast in saturated hydraulic parameters (e.g., a ratio of $\frac{K_{s,coarse}}{K_{s,fine}} \approx 1.5$) to prevent the creation of a typical dual-domain structure where preferential flow paths would

Table 1
*Material Properties for the Individual Materials (Those Marked With * From Bechtold, Haber-Pohlmeier, et al., 2011)*

Type	d_m^* (mm)	K_s^* (cm day^{-1})	α^* (cm^{-1})	N^*(−)	n_f (−)
Coarse (FH31)	0.35	3,888	0.035	8.0	0.31
Fine (F36)	0.165	2,496	0.0177	10.8	0.37

Note. d_m is the mean grain size, K_s the saturated hydraulic conductivity, α used in the van Genuchten Formulation and related to the inverse of the air entry pressure, N is a dimensionless van Genuchten parameter, and n_f is the porosity of the individual materials.

Table 2
Overview of Conducted Experiments With Constant Cycle Duration of t_{cycle} = 86,400 s, Showing Utilized Dyes (Eos = Eosine B, BB = Brilliant Blue FCF), Dye Injection Type (Injection), Pump Rate (Q_{Pump}), Duration (t_{solute}), and mass (m_{solute}) of Solute Application as well as Duration of Infiltration and Evaporation Rates (t_{inf}, t_{evap}), Measured Effective Bulk Density (ρ_{bulk}) and Effective Porosity (n_e)

#	Dye tracer	Injection	Q_{Pump} (cm^3 min^{-1})	t_{solute} (s)	m_{solute} (g)	t_{inf} (s cycle^{-1})	t_{evap} (s cycle^{-1})	ρ_{bulk} (g cm^{-3})	n_e (–)
1	Eos	Single	0.013	33,640	7.5	86,400	0	1,653	0.36
2	Eos	Single	2	228	7.6	985	85,415	1,651	0.36
3	Eos	Single	9	51	7.7	220	86,180	1,614	0.36
4	Eos and BB	Mixed	9	51	7.7	220	86,180	1,659	0.36
5	Eos and BB	Paths	0.013	33,640	7.5	86,400	0	1,682	0.34
6	Eos and BB	paths	2	228	7.6	985	85,415	1,643	0.35
7	Eos and BB	Paths	10	46	7.7	150	86,250	1,657	0.35

be determined mainly by material properties under saturated conditions. Typical consequences of preferential flow such as early solute breakthrough and pronounced tailing resulting from material heterogeneity alone were thus not expected to occur under saturated conditions. For our experiments, comprising heterogeneous packings, the effective bulk density ρ_{bulk} and effective porosity n_e were determined by weighting the flow cell alone, filled with dry and filled with the fully saturated porous media. Both measures showed to be well reproducible for all investigated experiments as listed in Table 2.

2.1.3. Initial and Boundary Conditions

Throughout different experiments listed in Table 2, varying forcings (infiltration or evaporation) were applied on the open topside of the flow cell by changing between an irrigation head and a fan. Freshwater (either with or without solute) was applied at the soil surface by an irrigation head with eight tubes (d = 0.04 cm). To achieve a spatially uniform application of water and solute, the tubes were evenly distributed over the width of the flow cell, and each tube was connected separately to a peristaltic pump which was calibrated before each experiment for optimal accuracy of flow rates. The outlets of the irrigation head were installed close (≈0.5 cm) to the porous medium surface to avoid formation of drop impact craters as these could possibly alter subsequent infiltration and evaporation behavior. Infiltration rates in all experiments were chosen such that they did not exceed the infiltration capacity of the heterogeneous medium such that no accumulation of water at the soil surface occured. For steady-state infiltration experiments (Table 2, experiments 1 and 5), the irrigation head was connected to the flow cell and sealed such that no evaporation could occur. For dynamic experiments which comprised evaporation, a fan (d = 12 cm) was installed approximately 3 cm above the surface of the porous medium to create a turbulent boundary layer and enhance evaporation. The flow cell lower outlet was connected to an overflow reservoir with a constant water level to keep the pressure head at the bottom of the flow cell constant at −10 cm (Figure 1). The overflow reservoir was sealed to prevent evaporation from it.

Before each experiment, the flow cell was slowly saturated from the bottom (through the flow cells outlets) via a peristaltic pump that created a constant inflow. Afterward, the setup was allowed to equilibrate to a pressure head of −10 cm at the bottom of the domain for at least 1 day. Equilibrium water contents under the beforementioned initial condition obtained from radiographic measurements are shown in Figure 2 (panels a and b) along with water content and unsaturated hydraulic conductivity (panels c and d) derived from van Genuchten parametrization with the parameters listed in Table 1. Due to lower capillary forces of the coarse sand, water content and consequently unsaturated hydraulic conductivity decreased stronger with distance from the imposed water table than in the fine sand, resulting in an intersection of hydraulic conductivity curves in Figure 2d.

In order to achieve controlled evaporation rates, all experiments were conducted in a climatized laboratory with almost constant temperature and humidity. Temperatures were monitored via three separate thermometers throughout all experiments and stayed around 26°C with a deviation of ±2°C. The relative humidity (measured by a hygrometer) ranged from 40% to 50%. An overview of the applied boundary conditions comprising infiltration and evaporation durations for each experiment along with application duration is listed in Table 2. It should be noted that all experiments comprised the same cycle duration of 1 day. Infiltration flow rates and durations are chosen such that the total water volumes that infiltrated in one cycle were (theoretically) identical throughout all experiments. This means that net infiltration rates were

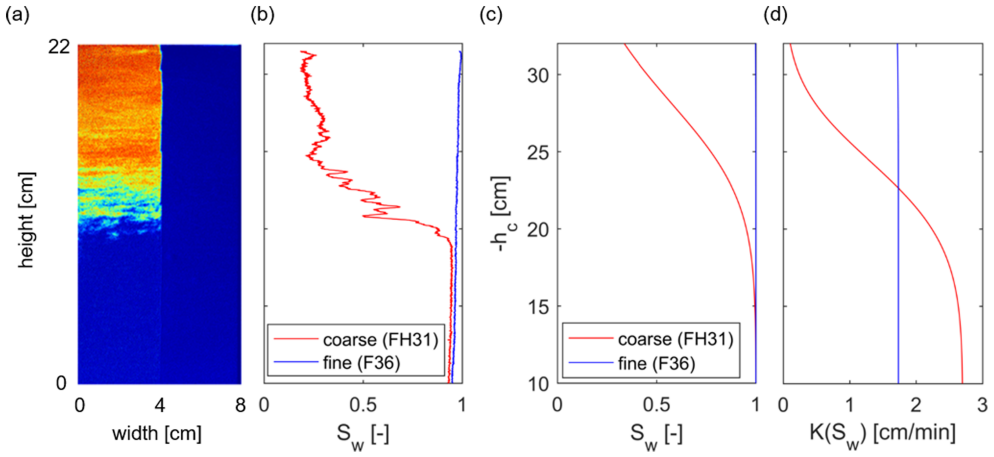

Figure 2. Laboratory measured (a) distribution of relative water saturation (red = low, blue = high) and (b) horizontally averaged relative saturations for each material in hydrostatic equilibrium for $h(z = 0) = -10$ cm obtained from radiography. (c) Saturation versus negative pressure head and (d) unsaturated hydraulic conductivities versus negative pressure head obtained with van Genuchten relationship parameterized with values from the literature (Bechtold, Haber-Pohlmeier, et al., 2011) given in Table 1.

planned to be the same in all experiments. However, slight deviations in infiltration and evaporation rates did occur as both were not perfectly controllable.

To obtain information about solute transport, dye tracers in low concentrations, which do not alter the density of the freshwater in which they are dissolved, were utilized. Thereby, we prevented the occurrence of density-driven flow, which would have complicated the correct interpretation of the role of upward flow during evaporation. We used dye tracers Eosine B (Eos) and Brilliant Blue FCF (BB) to visualize transport patterns and obtain breakthrough curves. The initial solute concentration within the flow cell for all experiments was zero before $\approx$7.5 cm^3 dye tracer solution with a concentration of $C_0 \approx 0.0625$ g cm^{-3} was applied at the porous medium surface via an irrigation head during the first time steps of each experiment. The time of solute (t_{solute}) application for each experiment is listed along with infiltration (t_{inf}) and evaporation (t_{evap}) durations in Table 2. The cycle duration (t_{cycle}) of 1 day was kept constant throughout all experiments. We carried out experiments where (i) a single Eosine tracer (Table 2, experiments 1–3) or (ii) a mixture of Eosine and Brilliant Blue (Table 2, experiment 4) was applied uniformly on the entire soil surface and (iii) experiments where Eosine was applied to the surface of the coarse and Brilliant Blue to the fine material (Table 2, experiments 5–7).

2.2. Observations Related to Flow and Transport

2.2.1. Flow measurements

Fluxes in and out of the flow cell were monitored with two scales, where one supports the flow cell and the other one supports the overflow reservoir. An increase in weight of the reservoir corresponded to an outflow at the lower boundary of the flow cell, whereas a decrease of reservoir weight corresponded to an inflow through the lower boundary into the domain. Evaporation from the porous medium surface was determined from the cumulative weight loss of the reservoir and flow cell.

The pressure at the bottom boundary was constantly monitored throughout all experiments by a pressure sensor (Keller PR-41X). Only small pressure head deviations of $\pm$0.3 cm around the desired value of -10 cm were observed.

2.2.2. Spectroscopic Measurements

Solute breakthrough was quantified via absorption measurements with a nanophotometer (Type Implen C40) in a suprasil quartz glass flow through cell (Type Hellma 178.010.QS) with a very small (80 μl) volume and a pathlength (d [L]) of 10 mm installed directly below the bottom outlet of the flow cell. Solute concentrations were related to measured absorption (Abs [-]) by the Lambert-Beer Law (equation (1))

$$Abs = ln\left(\frac{I_0}{I}\right) = \epsilon \cdot C \cdot d, \tag{1}$$

where I_0 (−) and I are the incident and transmitted intensity of light passing through the sample, C (M·L^{-3}) is the solute concentration, and ϵ (L^2·M^{-1}) is the extinction coefficient for a certain wavelength λ. To test linearity between absorption and concentration and for the calculation of ϵ, calibration curves for Eosine and Brilliant Blue were obtained from dilution series comprising eight samples, spanning 2 orders of magnitude in concentration. Long-term stability, for example, regarding photolytic decay of the samples, was tested in spectroscopy measurements over the course of 2 weeks. No significant decay was found to occur during this period under the given laboratory conditions. Absorption was measured for wavelengths between 200 and 900 nm, and the absorption maximum in our measurements was found at 520 (±1) nm for Eosine and 629 (±1) nm for Brilliant Blue, which is in good agreement with textbook values (French, 1927; Leibundgut et al., 2009). The pH values of the utilized water and solutions were measured for freshwater and source dye tracer solution as well as effluent solution and showed only slight deviations around 8.2 (±0.2) throughout the experiments.

During our experiments, time steps for absorption measurements differed with regard to flow velocities. For higher flow velocities (during infiltration and shortly after), measurement intervals were chosen shorter ($\Delta t = 10$ s) to capture the solute breakthrough in as much detail as possible, whereas for evaporation periods with lower flow velocities, the interval was increased ($\Delta t = 1,800$ s).

2.2.3. Photographic Images

In addition to quantitative breakthrough, solute distribution over time within the domain was monitored qualitatively via photographic (RGB) images to provide qualitative evidence of local solute transport processes and facilitate the interpretation of the breakthrough curves. A DSLR Camera (Nikon D90) and flow cell were set up at a constant distance for all experiments resulting in an image resolution of 172 pixels per centimeter. Uniform lighting was achieved by using an 59 by 59 cm^2 LED panel with a color temperature of 4,000 K.

2.3. Evaluation of Measurements

2.3.1. Breakthrough Curves

We evaluated solute breakthrough under dynamic boundary conditions by joint consideration of measurements of flow rates, directions, and concentrations at the bottom of the flow cell. Solute recovery rates (RR) (Maloszewski et al., 1999) over time and cumulative water outflow were calculated for each tracer under consideration of the injected dye tracer mass (M [M]) by equation (2)

$$RR(t) = \frac{1}{M}\int_0^t C(t)\cdot Q_w(t)\,\mathrm{d}t, \tag{2}$$

where $C\,(M\,L^{-3})$ is the ultraviolet visible measured concentration and $Q_w\,(L^3T^{-1})$ is the water flow derived from scale measurements, which changes its sign with flow direction. Both were obtained at a certain time step $t\,(T)$.

As two different dyes are utilized in this manuscript, a test of their comparability under representative conditions was an important prerequisite for further studies. Therefore, we carried out a dynamic experiment (#4) where we applied a mixture of Eosine and Brilliant Blue (ratio 1:1) and evaluated the solute recovery rate of both tracers. In Figure 3a, solute recovery rates for the individual dyes are evaluated with regard to the cumulative water outflow.

Recovery rates show only minor discrepancies between both tracers. Generally, arrival of Brilliant Blue is delayed slightly compared to Eosine, possibly indicating stronger sorption of Brilliant Blue. However, this effect is small enough to be omitted in the current scope. Hence, we found the tracers suitable for direct comparison.

Regarding solute recovery, it is again important to note that changes in water flux direction between infiltration and evaporation allow for either increase or decrease of cumulative outflow as well as revovery rate (meaning water and solute flow back into the domain). This is illustrated in Figure 3b where measurements with larger spacing were obtained during infiltration and seemingly continuous measurements (due to their close proximity in terms of cumulative flux and solute recovery, indicating only small changes over time due to low evaporation rates) were obtained during evaporation. Additionally, Figure 3b is also suited to verify the accuracy of both water and concentration measurements as the inflowing solute mass was always equal to the outflowing solute mass. In Figure 3b, small arrows indicate inflow

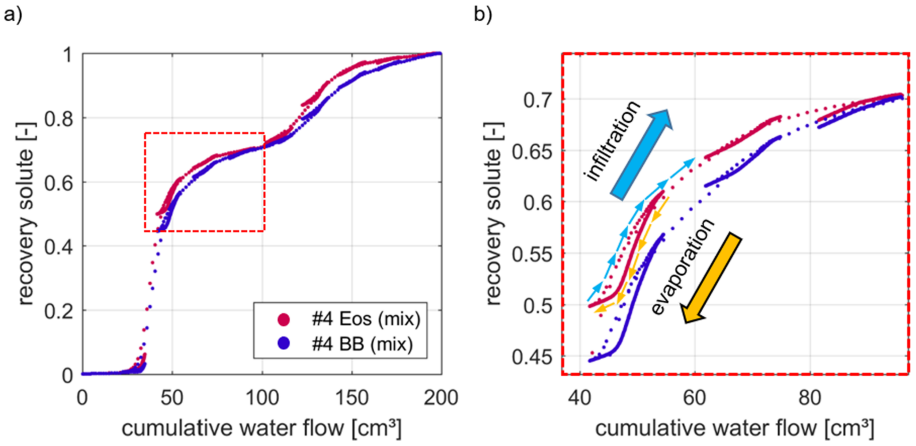

Figure 3. (a) Solute recovery versus cumulative water flux for Eosine and Brilliant Blue injected in mixture in experiment 4 (Table 2). (b) Zoom of (a) illustrating increasing cumulative water flow and solute recovery during infiltration and decreasing under evaporation. In (b), measurements with large spacings correspond to those obtained during infiltration, whereas lines correspond to those obtained during evaporation.

(orange) and outflow (light blue) from the domain for Eosine dye forming closed "loops" (for Brilliant Blue, the same is valid but not indicated in Figure 3b).

2.3.2. Dye Distribution in the Domain

The dye tracer distribution within the domain at multiple time steps was retrieved qualitatively from image analysis for all experiments. We used Matlab in combination with the image processing software ImageJ (Schneider et al., 2012) to eliminate distortion, reflections, and background noise from the recorded RGB images and enhance visibility of the utilized dye tracers. Our correction procedure consisted of four general steps, namely, (i) geometric correction of the original images to correct distortion, (ii) cropping to relevant area of the flow cell, (iii) flat field correction of all images obtained during the experiment ($i_{\mathrm{exp}}(t)$) with a reference image (i_{ref}) and its mean intensity (k) obtained prior to solute application by

$$i_{\mathrm{corr}}(t) = \frac{i_{\mathrm{exp}}(t)}{i_{ref}} \cdot k \tag{3}$$

(Landini, 2006-2014); flat field correction serves to remove static background noise and reflections; and (iv) application of histogram stretching comprising a cutoff fraction of 0.3% of pixels to enhance image contrast. This correction procedure has been applied successfully before (Cremer et al., 2017) and is similar to those utilized by Zinn et al. (2004) and Luo et al. (2010).

After this general correction procedure, RGB channels of the images were split, and dye specific image enhancements are conducted. For Eosine, which absorbs strongest in the green and least in the red channel, the prior was subtracted from the latter to further decrease image noise. For Brilliant Blue, this procedure was performed analogous considering the blue and red channel. Subsequently, we used a median filter with a radius of 0.15 cm to smooth concentration distributions.

A direct calculation of local concentration from the images was not possible, as a linear relation between color signal (RGB values) and concentration cannot be expected. Instead, from the corrected images, spatial moments were calculated under consideration of the image scale by first thresholding to divide the image into foreground (where solute is present) and background (where no detectable solute exists). Hereby, the foreground was computed separately for each present solute. Subsequently, first-order spatial moments (center of mass in horizontal (x) and vertical (z) direction) were calculated from the brightness-weighted average of the x and z coordinates of the foreground selection with regard to their initial center of mass x_0 directly after application and distance from the bottom of the flow cell (z_0). This means, we used an indicator field (I(x,z)) as substitute for the concentration field. First-order spatial moments are defined as

$$com_x = \frac{\int_{A_{\mathrm{cell}}} (x - x_0) I(x,z) \mathrm{d}x\mathrm{d}z}{\int_{A_{\mathrm{cell}}} I(x,z) \mathrm{d}x\mathrm{d}z}, \tag{4}$$

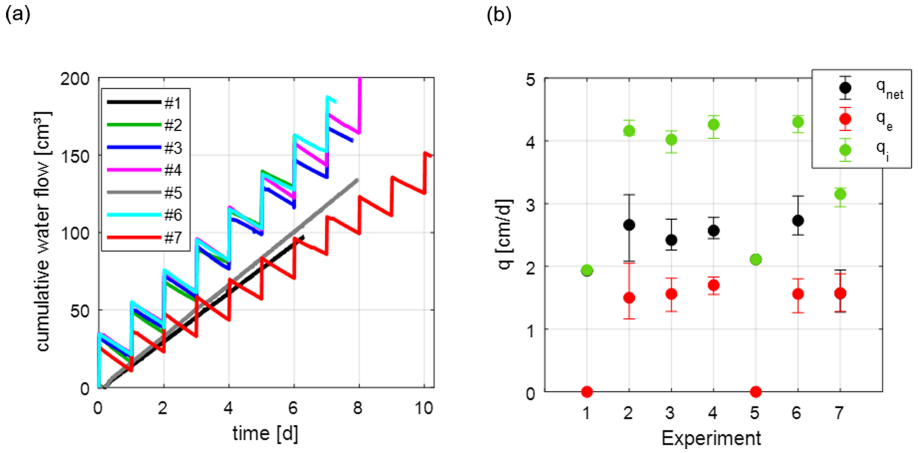

Figure 4. (a) Cumulative water flow versus time at the lower boundary of the flow cell for all experiments (numbers refer to experiments in Table 2). Increasing cumulative water flow indicates outflow from the flow cell during infiltration; decreasing values indicate inflow during evaporation from the porous medium surface. (b) Daily averaged flow rates for infiltration (q_i), evaporation (q_e), and resulting net flow rate (q_{net}). Error bars in (b) indicate minima and maxima of flow rates for individual cycles.

and

$$com_z = \frac{\int_{A_{cell}} (z - z_0) I(x,z) \mathrm{d}x\mathrm{d}z}{\int_{A_{cell}} I(x,z) \mathrm{d}x\mathrm{d}z}. \quad (5)$$

While spatial moments obtained from these indicator fields will likely differ from moments that would be obtained from concentration distributions, the moments computed here are however useful for the comparison of different experiments.

3. Results

To identify the implications of dynamic boundary conditions on miscible solute transport, we conducted and analyzed the laboratory experiments listed in Table 2. As solute transport is directly influenced by water fluxes, we begin this section with a short evaluation of water fluxes and flow paths.

3.1. Water Flow

Cumulative water flow through the bottom boundary of the flow cell over time is presented in Figure 4a.

Sections of local linear decline of curves for dynamic experiments (2, 3, 4, 6, and 7) in Figure 4a indicate temporally constant evaporation rates, characteristic for liquid flow dominated ("Stage 1") evaporation conditions. Averaged flow rates for each experiment separated into infiltration, evaporation, and net shares are illustrated in Figure 4b along with their maximum deviations (during specific infiltration or evaporation events) as error bars.

Resulting flow paths for a steady-state (5) and two dynamic experiments (6 and 7) were visualized by injection of different dyes at the surface of each material and illustrated as temporal sequences of images in Figure 5.

During infiltration, for the steady-state and mild dynamic experiment (Rows 1 and 2 of Figure 5), lateral flow close to the soil surface from coarse to fine material occured, as indicated in the images by Eosine displacing Brilliant Blue. This lateral flow can be attributed to lower water potential in the fine material. As the coarse materials saturation and hydraulic conductivity increased with distance from the soil surface (toward the imposed water table), it eventually exceeded the hydraulic conductivity of the fine material (at intersection point in Figure 2d). Consequently, this led to a lateral flow from fine to coarse material in the lower half of the domain at a height corresponding to the intersection point of hydraulic conductivity curves, thus forming an s-shaped flow path. During evaporation in experiment 6, the flow paths reversed, leading to flow from coarse to fine material at the approximate height of the intersection point of hydraulic conductivity curves

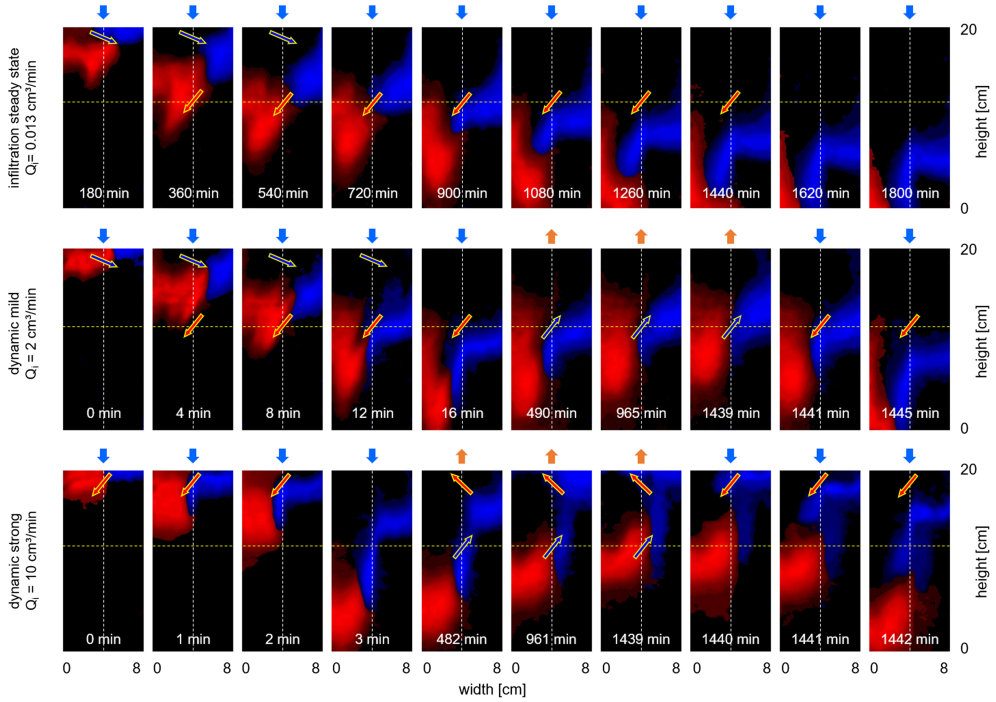

Figure 5. False-color plots of Eosine (red, applied to coarse) and Brilliant Blue (blue, applied to fine) distributions obtained from RGB images for three different experiments (5–7) as time series. First row for Steady-State Infiltration experiment 5, second row for dynamic experiment with mild infiltration rate (experiment 6), and last row for dynamic experiment (7) with a strong infiltration rate. Arrows above the images indicate active upper boundary condition (infiltration or evaporation). Vertical dashed lines indicate the approximate position of the material interface, whereas horizontal dashed lines indicate the approximate position of the intersection point.

and flow from fine to coarse close to the soil surface due to the constant evaporation flux at the surface. In Figure 5, the approximate position of the intersection point is indicated by horizontal dashed lines and that of the material interface by vertical dashed lines.

The infiltration path for dynamics with strong infiltration (experiment 7, last row of Figure 5) differed from the other experiments. This can be explained by an infiltration flux which approximated or exceeded the infiltration capacity of the fine material, thus resulting in a lateral flow from fine to coarse in the vicinity of the soil surface. The wet coarse sand has a higher hydraulic conductivity than the fine sand. Hereby, infiltration fluxes largely bypassed the upper regions of the fine material resulting in low vertical flow velocities in this domain. In Figure 5 (third row), this is captured by Brilliant Blue displacing Eosine in the coarse material and a visibly large variance in vertical flow velocities between coarse and fine material. Upward flow in this experiment followed the same paths as those already outlined for experiment 6 during evaporation. Hereby, for experiment 7, or more generally for experiments with strong infiltration fluxes, flow paths between infiltration and evaporation are not reversed but differ.

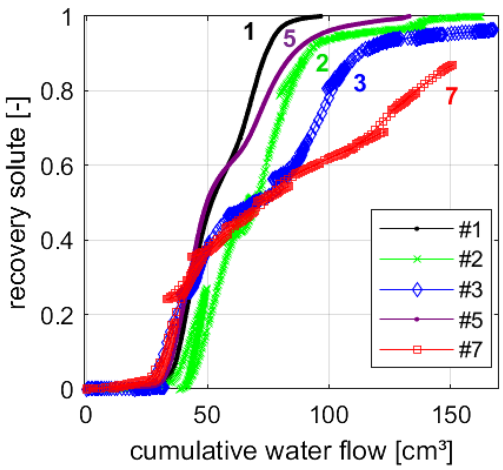

Figure 6. Solute recovery versus cumulative water flux for two steady-state experiments (1 and 5) and three transient experiments (2, 3, and 7).

3.2. Solute Transport

Solute recovery was evaluated at the bottom of the domain for two steady-state (1 and 5) and three dynamic (2, 3, and 7) experiments and is presented in Figure 6.

For experiments comprising multiple dyes (5 and 7), the total recovery is herein calculated from an arithmetic mean of the dyes individual breakthroughs. To allow a direct comparison of experiments independent of the temporal variations in water flux resulting from different boundary

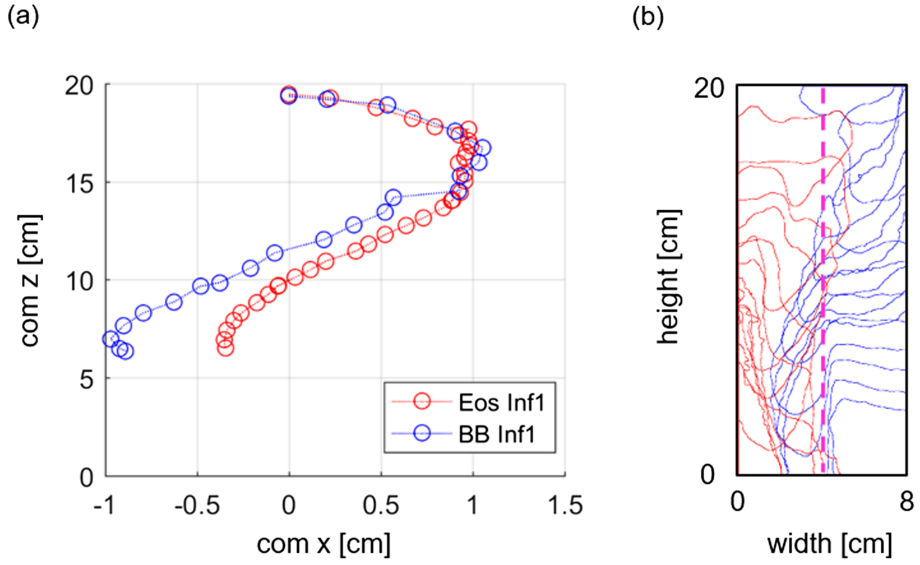

Figure 7. (a) Center of mass (com) in vertical (z) and horizontal (x) directions for Eosine and Brilliant Blue in Steady Infiltration experiment 5. (b) Isolines for both tracers (Eosine applied to coarse and Brilliant Blue to fine material) during consecutive time steps (solute moving from top to bottom of the domain). The dashed line in (b) indicates the position of the material interface.

conditions, the amount of recovered solute is here plotted over cumulative water outflow (note that experiment 6 of Table 2 could not be evaluated in terms of solute breakthrough due to a malfunction of the spectrometer).

In Figure 6, the initial breakthrough of the two steady-state experiments (1 and 5) showed to be well reproducible. The second breakthrough and tailing in experiment 5 is slightly more pronounced. This difference in recovery behavior is most likely the result of slight differences in infiltration fluxes between experiments (see Figure 4) or small differences in sand packings (e.g., n_e in Table 2). Experiments comprising strong dynamic boundary conditions, referring to strongest infiltration rates over the shortest infiltration period and longest evaporation period (3 and 7), experience a breakthrough distinct from those under steady-state infiltration (1 and 5) and mild dynamic boundary conditions (2). While deviations such as the general tendency for earlier first solute breakthrough exist in experiments with strong dynamic, the most prominent feature distinguishing these experiments from the others is the tailing (Figure 6). Tailing is mostly absent

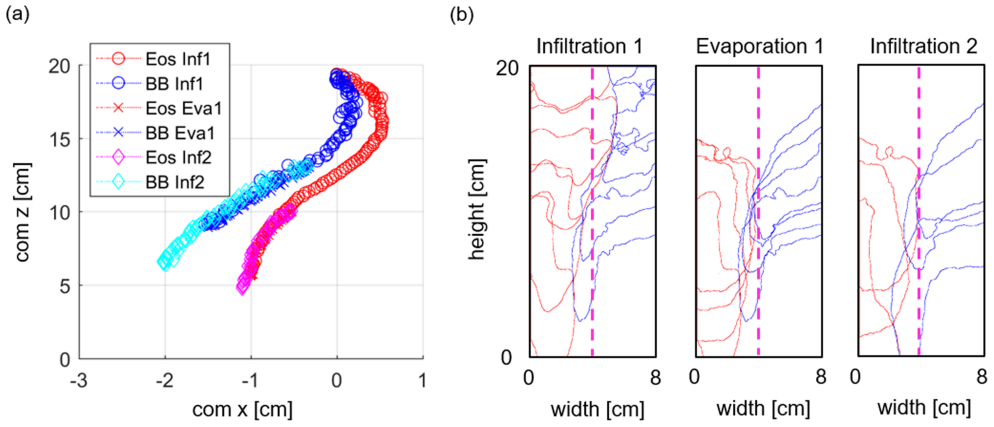

Figure 8. (a) Center of mass (com) in vertical (z) and horizontal (x) directions for Eosine and Brilliant Blue for Mild Dynamic experiment 6. Different infiltration and evaporations are indicated by varying colors and markers. (b) Isolines for both tracers (Eosine applied to coarse and Brilliant Blue to fine material) during consecutive time steps of infiltrations (solute moving downward in the domain) and evaporation (solute moving upward). Dashed lines in (b) indicate the position of the material interface.

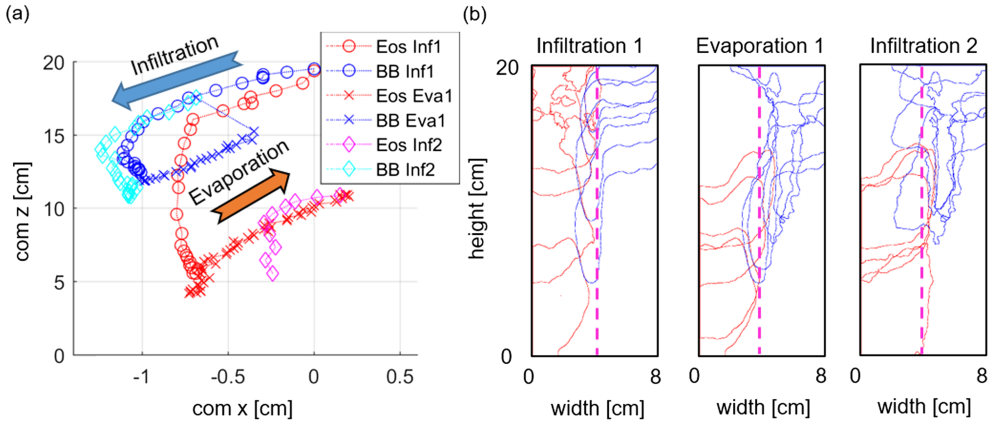

Figure 9. (a) Center of mass (com) in vertical (z) and horizontal (x) directions for Eosine and Brilliant Blue for Mild Dynamic experiment 7. Different infiltration and evaporations are indicated by varying colors and markers. (b) Isolines for both tracers (Eosine applied to coarse and Brilliant Blue to fine material) during consecutive time steps of infiltrations (solute moving downward in the domain) and evaporation (solute moving upward). Dashed lines in (b) indicate the position of the material interface.

in steady-state (1 and 5) and mild dynamic (2) experiments that show a similar solute recovery behavior in terms of solute recovery rates (steepness of graphs in Figure 6). Note that the slightly retarded first breakthrough for experiment 2 compared to others can be attributed to an air bubble in one outlet below the coarse material which was flushed out during the first infiltration. Tailing becomes increasingly pronounced for experiments with dynamic boundary conditions that comprised the strongest infiltration rates and longest evaporation periods (3 and 7) (Figure 6). Comparing results of experiments 3 and 7, in which the latter comprised a slightly higher infiltration rate, a transition from a double breakthrough curve in experiment 3 to a strong initial breakthrough followed by a long, continuous tailing in experiment 7 is visible.

Responsible for the observed tailing are the differences between downward and upward flow paths discussed in Section 3.1. For steady-state (1 and 5) and mild dynamic (2) experiments, advective transport on an s-shaped flow path through both materials leads to a similar solute recovery (Figure 6). In order to help the interpretation of the solute recovery curves and to investigate redistribution through the material interface, the center of mass (com) in horizontal (x) and vertical (z) direction is evaluated in Figures 7a, 8a, and 9a.

While the evaluation was performed at identical time steps for both dyes within one experiment, time steps differed between experiments in order to account for differing transport time scales. Thus, relative velocities of Eosine and Brilliant Blue can be compared. Horizontal (x) components of the center of mass were normalized with regard to the initial center of mass (x_0) of the respective tracer directly after injection. The initial center of mass for Eosine and Brilliant Blue was located at the center of the individual materials to which the tracers have been applied. Transport paths for steady-state and mild dynamic experiments are the same and align with the s-shaped form of the flow paths (Figures 7a and 8a). Hence, from the center of mass in vertical and horizontal directions evaluated individually for each tracer, it becomes apparent that transport paths of the solute are almost identical for steady-state and mild dynamic experiments (Figures 7a and 8a). This is also evident from the temporal evolution of the isolines presented in Figures 7b and 8b. As indicated by (overlapping markers for) the center of mass in Figure 8a, solute transport in experiments with mild dynamic was precisely reversed between an infiltration (where the vertical center of mass is shifted downward over time) and succeeding evaporation (upward shift in vertical center of mass). This precise reversal of transport leads to comparable breakthrough over cumulative outflow for mild dynamic and steady-state experiments (Figure 6).

Experiments with a strong dynamic, as already evidenced by tailing in the breakthrough curves (Figure 6), differed in solute transport mechanisms from those with steady-state infiltration or mild dynamic. The center of mass for Eosine and Brilliant Blue in a strong dynamic experiment (7) in Figure 9a illustrates that transport was not reversed between infiltration and evaporation periods. In strong dynamic experiments, infiltration leads to significantly higher downward transport velocity for Eosine compared to Brilliant Blue resulting in a larger overall vertical spread of solute (Figure 9a). Brilliant Blue in this experiment was to a

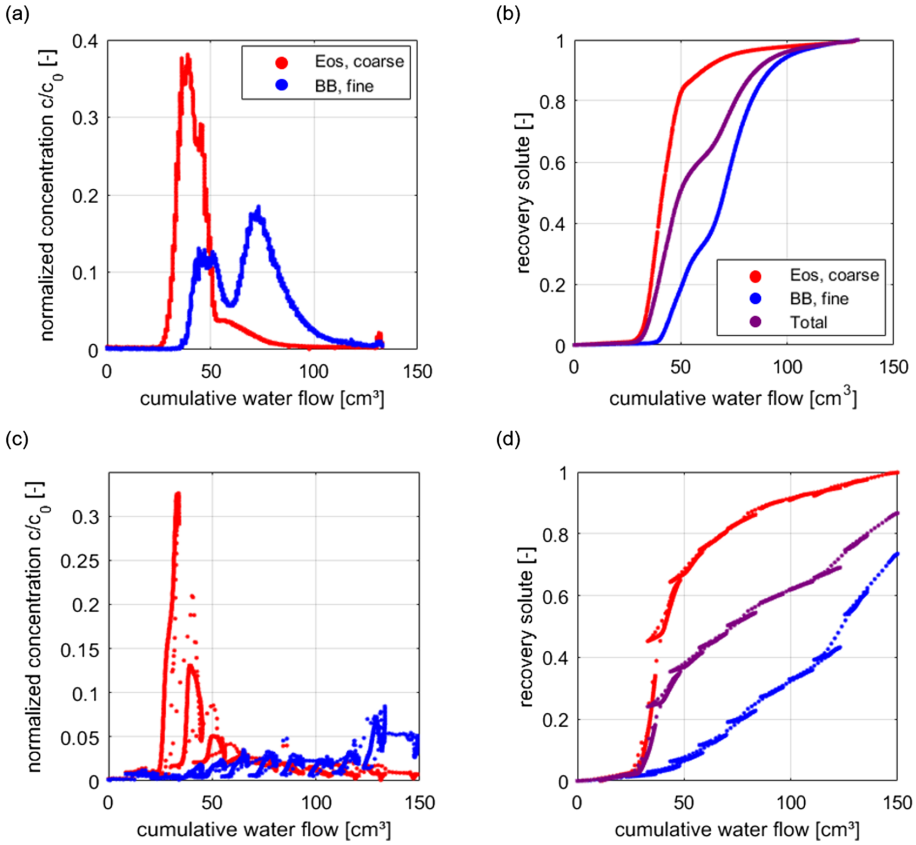

Figure 10. Normalized Eosine (Eos) and Brilliant Blue (BB) concentrations (a,c) and recovery (b,d) for Steady-State Infiltration experiment 5 (a,b) and Dynamic experiment 7 (c,d) versus cumulative water flow.

major extent trapped in the upper regions of the fine material by equally strong upward and downward fluxes in this domain, indicated in isolines during infiltration and evaporation (Figure 9b) and slow vertical velocities compared to Eosine (Figure 9a). This trapping of Brilliant Blue in the fine material is also well visible in the false-color plots of Figure 5 (last row) where the Brilliant Blue plume in the fine material at the end of the first infiltration (Picture 4) and at the end of the second infiltration (last picture) is located at approximately the same vertical position. Downward transport and leaching of Brilliant Blue in this experiment mainly occurred in the vicinity of the material interface and was strongly delayed compared to leaching in other experiments as the changing downward and upward flow paths resulted in a net flux close to zero in the fine material.

Strong dynamic boundary conditions in this experiment (7) thereby effectively trapped parts of the solute and delayed leaching of the trapped portions. It is herein important to note that trapping in the fine material in our experiments did not exclusively result from structural heterogeneity, as in the case of classical dual-domain structures which induce preferential flow (Gerke & van Genuchten, 1993), but rather from an interplay of dynamic boundary conditions and dynamically changing hydraulic properties of the porous medium.

Evaluation of the solute breakthrough and cumulative solute recovery for individual dyes for steady-state experiment (5) and strong dynamic experiment (7) (Figure 10) yields further quantitative information about the transport paths.

For the steady-state experiment, the s-shaped transport path passing through both materials resulted in similar first arrival times for Eosine and Brilliant Blue where the latter is solely slightly delayed (Figure 10a). Generally, arrival times of Brilliant Blue (fine material) and Eosine were similar in these experiments. Breakthrough for the strong dynamic experiment (Figure 10c) yields a Eosine peak arrival time almost identical to that under steady-state infiltration. However, lower Eosine peak concentrations in the strong

dynamic experiment (Figures 10a and 10c) and enhanced tailing of Eosine (Figures 10b and 10d) compared to the steady-state case indicate that besides Brilliant Blue, also a part of the Eosine was trapped due to dynamic boundary conditions. This observation indicates the capability of dynamic boundary conditions to affect solute transport paths so that solute which is initially not located in a trapping zone becomes trapped.

4. Summary, Conclusions, and Discussion

4.1. Summary of the Experiments

We presented a laboratory study of solute transport in variably saturated, heterogeneous porous media under dynamic boundary conditions. To assess the implications of dynamic boundary conditions for solute transport, experiments comprising cycles of infiltration and evaporation were compared to experiments in which a steady-state infiltration of similar net flow rate was applied at the soil surface. Intensity (rates) and durations of infiltration and evaporation were varied between dynamic experiments. By staining the infiltration flux with dye tracers Eosine and Brilliant Blue, transport in the domain was visualized and quantitatively assessed by calculation of spatial moments in an image analysis and spectroscopic measurements of the leached concentrations.

Especially in experiments in which high infiltration flow rates (approaching the materials hydraulic conductivity) were applied, downward flow and transport differed from upward transport. In these experiments, dynamic boundary conditions were found to affect flow and solute transport particularly strong as a region of the fine material was bypassed by portions of the flow during infiltration. In this bypassed region, over a cycle, this leads to almost balanced local upward and downward fluxes forming a quasi-stangnant zone. During evaporation, lateral redistribution of solute into this zones of the fine material in the vicinity of the soil surface resulted in trapping herein. Regarding solute breakthrough, trapping of solute manifested in solute breakthrough with pronounced tailing. The experiments thus illustrate that dynamic boundary conditions can result in changing flow patterns during upward and downward flow, which can cause local trapping of transported substances. Key factors determining if a change of flow pattern occurs between upward and downward flow are the individual materials' local unsaturated hydraulic conductivity and the applied flow rates. When infiltration flow rates exceed the saturated hydraulic conductivity of the fine material in the vicinity of the soil surface, fast preferential downward directed transport occurs in the coarse material and flow effectively bypasses the fine material. This relates to a retardation of leaching trapped in the fine material into deeper zones, which in the current study is captured as enhanced tailing in the breakthrough curves. The trapping effect is found to be enhanced under conditions of strong and short infiltration followed by longer evaporation periods.

As materials in our study were chosen deliberately for their small parameter contrast (e.g., a ratio of $\frac{K_{s,coarse}}{K_{s,fine}} \approx 1.5$), trapping in the experiments did not originate from stagnant zones formed by classical dual-domain heterogeneous structure (i.e., where strong differences in saturated hydraulic conductivities between two materials lead to preferential flow in small parts of the soil while the rest remains stagnant). Instead, our study demonstrates trapping of solute and retardation of solute leaching manifesting primarily as an effect of dynamic boundary conditions.

The findings of the experiments shown here have possible implications for the transport of dissolved substances in the vadose zone. Trapping due to naturally occurring dynamic boundary conditions between hydraulically similar porous media yields longer residence times of solutes in the root zone and retarded leaching into deeper soil layers and ultimately the groundwater.

In order to predict solute leaching from classical dual-domain material structures as they are utilized in this study, typically dual-domain models such as the one proposed by Gerke and van Genuchten (1993) would be utilized. Therefore, in the following, concluding subsection we briefly elaborate that, while the recovery of the investigated steady-state infiltration experiment (1) of this study can be matched well with an upscaled dual-domain model, a numerical (upscaled) representation of recovery observed in the laboratory under dynamic boundary conditions is problematic.

4.2. Prediction of Laboratory Measured Recovery With Double-Continuum Models

To assess if the laboratory measured recovery rates can be estimated with an upscaled, dual-domain model, we resimulate the laboratory experiments using the public domain model environment HYDRUS 1D (Simunek & van Genuchten, 2008).

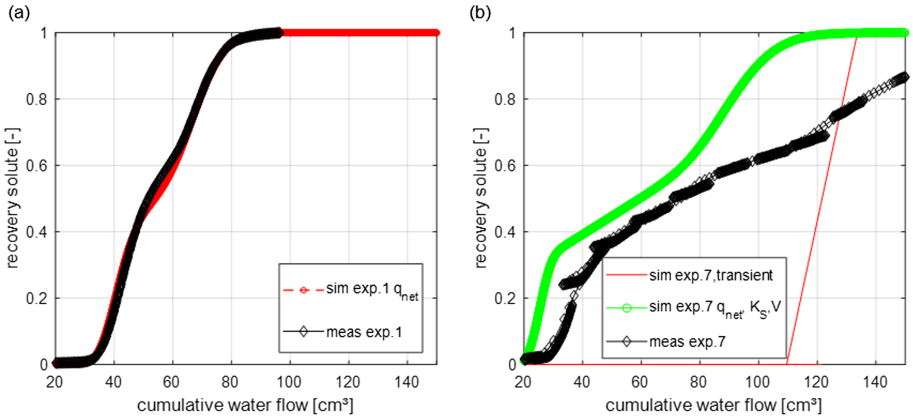

Figure 11. Solute recovery versus cumulative water flux compared to measured recovery of experiment 1 (a, left) and experiment 7 (b, right).

An upscaled model of dual-permeability type comprising two domains, subsequently referred to as matrix and fracture, in which Richards-flow and advective-dispersive solute transport is solved separately for each domain (Gerke & van Genuchten, 1993) is chosen for this purpose. The chosen model is capable to simulate water flow and solute transport in two separate 1-D domains and water as well as (solute) mass transfer between them. A more detailed description of the model and parameters can be found in Appendix A.

Three simulation results are shown in Figure 11. The result of a simulation comprising the steady-state infiltration net flow rate of experiment 1 is compared to the measured solute recovery of experiment 1 on the left in Figure 11a. The laboratory measured recovery of Steady-State experiment 1 (diamonds, black) is matched very well by the numerical resimulation (dotted, red) regarding initial breakthrough and tailing. Merely in the transition from first (fracture) to second (matrix) breakthrough, slight deviations between modeled and observed recovery are visible. The dynamic setting of experiment 7 (Table 2) is shown on the right in Figure 11b. In comparison to Figure 11a, it is obvious that a simulation with steady-state flow using the net infiltration rate would yield a poor prediction of the stronger tailing in the dynamic recovery curve of experiment 7.

Transient boundary conditions could be considered explicitly in the dual-permeability model; however, in the cases considered here, the simulations suffered from stability problems (see also Bechtold, Vanderborght, et al., 2011) or gave poor representations of the breakthrough curves. An example of transient recovery is shown for experiment 7 in Figure 11b where the measured is indicated by a black line with diamond markers and the transient simulation is shown as a red line.

In order to match the measured breakthrough curve under dynamic conditions using steady-state flow, a higher infiltration rate that matches the averaged flow velocity in the fast domain could be chosen. However, this approach would not generate the strong tailing found in the experiments (not shown). In addition, this approach would have the major drawback that it does not reproduce the right water balance and would, for example, overestimate groundwater recharge. An alternative would be to impose the net infiltration rate and to enforce earlier breakthrough and longer tailing by increasing the contrast of saturated hydraulic conductivity of the two domains and to impose the shape of the breakthrough curve by changing the volume percentages of the materials. In Figure 11b, a breakthrough curve generated with the net infiltration rate, where the contrast of hydraulic conductivities was increased by a factor of 3 and the volume percentage from coarse to fine material was changed from 0.5/0.5 to 0.3/0.7 compared to the steady-state case (of Figure 11a) is shown in Figure 11b (green line with circle markers). Choosing these parameters as effective parameters to capture the influence of the dynamic boundary conditions yields better predictions of the breakthrough curve. Naturally, the match could be improved further by changing also the exchange coefficients. However, how to predict such effective parameters from the material properties and boundary conditions is not clear. The question how to appropriately represent recovery under dynamic boundary conditions, as applied in this

manuscript, in effective models that do not require explicit description of the dynamic boundary conditions and the spatial soil patterns remains a topic for future research.

Appendix A: Detailed Description of the Dual-Permeability Setup

The simulation setup based on the laboratory setup comprises the same vertical domain extent of 22 cm. Material parameters in simulations are chosen identical to the measured parameters from Table 1. Solely, the van Genuchten α for the coarse sand is adjusted from 0.035 to 0.045 cm^{-1} to better represent the X-ray radiography derived saturation distribution shown in Figure 2 measured in current packings. Pumping rates from Table 2 are applied as water fluxes uniformly distributed at the surface of matrix and fracture. Solute application is considered as concentration flux boundary condition with an application starting at the first simulation time step and a duration corresponding to that of the respective laboratory experiment (t_{solute} in Table 2). A constant head and zero concentration gradient boundary condition are applied at the bottom of the domain. The longitudinal dispersivity in matrix and fracture are set to the mean grain size (d_m) of the individual materials which is common (Bechtold, Haber-Pohlmeier, et al., 2011). The molecular diffusion coefficient of solute in the simulation was chosen to be 6e−4 $cm^2\ min^{-1}$ in agreement with values reported for Brilliant Blue in the literature (Kasteel et al., 2002). Water transfer between matrix and fracture is modeled proportional to the difference of pressure heads between both domains (h_f and h_m for fracture and matrix, respectively) by a first-order rate equation (Gerke & van Genuchten, 1993):

$$\Gamma_w = \alpha_w(h_f - h_m) \text{ with } \alpha_w = \alpha_w^* K_{sa} \text{ where } \alpha_w^* = \frac{\beta}{a^2}\gamma_w. \tag{A1}$$

Γ_w is the water transfer rate (min^{-1}) and K_{sa} ($cm\ min^{-1}$) is the effective hydraulic conductivity of the fracture-matrix interface. The equation was parameterized here with values from the literature (Gerke & van Genuchten, 1996) where the shape parameter $\beta = 3$ for a rectangular two-dimensional slab was used. The scaling factor γ_w was set to 0.4 and the effective diffusion path length representing the distance from the center of the fine material (matrix) to the material interface (fracture boundary) to $a = 2$ cm according to the geometry of the laboratory experiment.

To couple solute transport between both domains, the solute transfer rate Γ_s is described by (Gerke & van Genuchten, 1996)

$$\Gamma_s = \alpha_s(1 - w_m)(c_f - c_m) + \Gamma_w c^* \text{ where } \alpha_s = \frac{\beta}{a^2}D_a, \tag{A2}$$

with the first-order solute mass transfer coefficient α_s and w_f the relative volumetric proportion of the fracture pore interface, which is chosen here to 0.5. c^* is equal to the fracture concentration (c_f) for $\Gamma_w > 0$ and equal to the matrix concentration (c_m) for $\Gamma_w < 0$. The two parameters, (i) the effective hydraulic conductivity of the fracture-matrix interface (K_{sa} [$cm\ min^{-1}$]) and (ii) the effective diffusion coefficient (D_a [$cm^2\ min^{-1}$]) for solute transfer between matrix and fracture, were fitted to optimize the match of the recovery curve of the Steady-State experiment 1. The best fit yielded K_{sa} = 1e−5 $cm\ min^{-1}$ and D_a = 9e−5 $cm^2\ min^{-1}$. These transfer parameters were kept constant in the other simulations.

Acknowledgments
This work was conducted in the context of the DFG Project FOR 1083 (NE 824/6-2): MUSIS (Multiscale Interfaces in Unsaturated Soil). The authors wish to thank the Deutsche Forschungsgesellschaft (DFG) for funding. We furthermore thank John Koestel and two further anonymous reviewers for a constructive discussion. Data statement: Data utilized in this manuscript is made publicly available online (http://www.hydroshare.org/resource/40344e265cef4dae989dca91e545d286).

References

Bechtold, M., Haber-Pohlmeier, S., Vanderborght, J., Pohlmeier, A., Ferre, P. A., & Vereecken, H. (2011). Near-surface solute redistribution during evaporation. *Geophysical Research Letters*, *38*, L17404. https://doi.org/10.1029/2011GL048147

Bechtold, M., Vanderborght, J., Ippisch, O., & Vereecken, H. (2011). Efficient random walk particle tracking algorithm for advective dispersive transport in media with discontinuous dispersion coefficients and water contents. *Water Resources Research*, *47*, W10526. https://doi.org/10.1029/2010WR010267

Bechtold, M., Vanderborght, J., Weihermueller, L., Herbst, M., Gunther, T., Ippisch, O., et al. (2012). Upward transport in a three-dimensional heterogeneous laboratory soil under evaporation conditions. *Vadose Zone Journal*, *11*(2), 1976–1982.

Cirpka, O. A., & Attinger, S. (2003). Effective dispersion in heterogeneous media under random transient flow conditions. *Water Resources Research*, *39*(9), 1257. https://doi.org/10.1029/2002WR001931

Cremer, C. J. M., Neuweiler, I., Bechtold, M., & Vanderborght, J. (2016). Solute transport in heterogeneous soil with time-dependent boundary conditions. *Vadose Zone Journal*, *15*(6). Retrieved from https://doi.org/10.2136/vzj2015.11.0144

Cremer, C. J. M., Schuetz, C., Neuweiler, I., Lehmann, P., & Lehmann, E. (2017). Unstable infiltration experiments in dry porous media. *Vadose Zone Journal*, *16*(7). https://doi.org/10.2136/vzj2016.10.0092

Dentz, M., & Carrera, J. (2003). Effective dispersion in temporally fluctuating flow through a heterogeneous medium. *Physical Review E*, *68*(3), 36310. https://doi.org/10.1103/PhysRevE.68.036310

French, R. W. (1927). Extinction coefficients of dyes. *Stain Technology*, *2*(4), 124–125.

Gerke, H. H., & van Genuchten, M. (1993). A dual-porosity model for simulating the preferential movement of water and solutes in structured porous media. *Water Resources Research*, *29*(2), 305–319. https://doi.org/10.1029/92WR02339

Gerke, H. H., & van Genuchten, M. T. (1996). Macroscopic representation of structural geometry for simulating water and solute movement in dual-porosity media. *Advances in Water Resources*, *19*(6), 343–357. https://doi.org/10.1016/0309-1708(96)00012-7

Kasteel, R., Pütz, T., Vanderborght, J., & Vereecken, Harry (2009). Solute spreading under transient conditions in a field soil. *Vadose Zone Journal*, *8*(3), 690. https://doi.org/10.2136/vzj2008.0024

Kasteel, R., Vogel, H. J., & Roth, K. (2002). Effect of non-linear adsorption on the transport behaviour of brilliant blue in a field soil. *European Journal of Soil Science*, *53*, 231–240. https://doi.org/10.1046/j.1365-2389.2002.00437.x

Landini, G. (2006-2014). How to correct background illumination in brightfield microscopy. Available online.

Lehmann, P., & Or, D. (2009). Evaporation and capillary coupling across vertical textural contrasts in porous media. *Physical Review E*, *80*(4), 46318.

Leibundgut, C., Maloszewski, P., & Kuells, C. (2009). *Tracers in hydrology*. Hoboken, NJ: Wiley. https://doi.org/10.1002/9780470747148

Luo, L., Lin, H., & Li, S. (2010). Quantification of 3-D soil macropore networks in different soil types and land uses using computed tomography. *Journal of Hydrology*, *393*(1-2), 53–64. https://doi.org/10.1016/j.jhydrol.2010.03.031

Maloszewski, P., Herrmann, A., & Zuber, A. (1999). Interpretation of tracer tests performed in fractured rock of the Lange Bramke Basin, Germany. *Hydrogeology Journal*, *7*(2), 209–218. https://doi.org/10.1007/s100400050193

Nachshon, U., Weisbrod, N., Dragila, M. I., & Grader, A. (2011). Combined evaporation and salt precipitation in homogeneous and heterogeneous porous media. *Water Resources Research*, *47*, W03513. https://doi.org/10.1029/2010WR009677

Rehfeldt, K. R., & Gelhar, L. W. (1992). Stochastic analysis of dispersion in unsteady flow in heterogeneous aquifers. *Water Resources Research*, *28*(8), 1944–7973. https://doi.org/10.1029/92WR00750

Roth, K. (1995). Steady-state flow in an unsaturated, 2-dimensional, macroscopically homogeneous, Miller-similar medium. *Water Resources Research*, *31*, 2127–2140.

Roth, K., & Hammel, K. (1996). Transport of conservative chemical through an unsaturated two-dimensional Miller-similar medium with steady state flow. *Water Resources Research*, *32*, 1653–1663.

Russo, D., & Fiori, A. (2008). Equivalent vadose zone steady state flow: An assessment of its capability to predict transport in a realistic combined vadose zone-groundwater flow system. *Water Resources Research*, *44*, W09436. https://doi.org/10.1029/2007WR006170

Russo, D., Zaidel, J., & Laufer, A. (1998). Numerical analysis of flow and transport in a three-dimensional partially saturated heterogeneous soil. *Water Resources Research*, *34*(6), 1451–1468.

Schlueter, S., Vanderborght, J., & Vogel, H.-J. (2012). Hydraulic non-equilibrium during infiltration induced by structural connectivity. *Advances in Water Resources*, *44*, 101–112. https://doi.org/10.1016/j.advwatres.2012.05.002

Schneider, C. A., Rasband, W. S., & Eliceiri, K. W. (2012). NIH Image to ImageJ: 25 years of image analysis. *Nature Methods*, *9.7*, 671–675.

Simunek, J., & van Genuchten, M. T. (2008). Modeling nonequilibrium flow and transport processes using HYDRUS. *Vadose Zone Journal*, *7*(2), 782–797.

van Dam, J. C., de Rooij, G. H., Heinen, M., & Stagnitti, F. (2004). Concepts and dimensionality in modeling unsaturated water flow and solute transport. In *Unsaturated-zone Modeling: Progress, Challenges and Applications*, Wageningen UR Frontis Series (Vol. 6, pp. 1–36).

Vanderborght, J., Kasteel, R., & Vereecken, H. (2006). Stochastic continuum transport equations for field-scale solute transport. *Vadose Zone Journal*, *5*(1), 184–203.

Wildenschild, D., & Jensen, K. H. (1999). Laboratory investigations of effective flow behavior in unsaturated heterogeneous sands. *Water Resources Research*, *35*(1), 17–27. https://doi.org/10.1029/98WR01958

Zinn, B., Meigs, L. C., Harvey, C. F., Haggerty, R., Peplinski, W. J., & Von Schwerin, C. F. (2004). Experimental visualization of solute transport and mass transfer processes in two-dimensional conductivity fields with connected regions of high conductivity. *Environmental Science and Technology*, *38*(14), 3916–3926. https://doi.org/10.1021/es034958g